Alkali-activated binders based on ground granulated blast furnace slag and phosphogypsum

DOI: 10.1016/j.conbuildmat.2019.04.194
Handle: http://hdl.handle.net/1942/28165

ALKALI-ACTIVATED BINDERS BASED ON GROUND GRANULATED BLAST FURNACE SLAG AND PHOSPHOGYPSUM

Katrijn GIJBELS[a]*, Remus Ion IACOBESCU[b], Yiannis PONTIKES[b], Sonja SCHREURS[a], Wouter SCHROEYERS[a]

[a] Hasselt University, CMK, Nuclear Technological Centre, Agoralaan, Gebouw H, 3590 Diepenbeek, Belgium

[b] KU Leuven, Department of Materials Engineering, Kasteelpark Arenberg 44, 3001 Leuven, Belgium

* Corresponding author: Katrijn GIJBELS

katrijn.gijbels@uhasselt.be, remusion.iacobescu@kuleuven.be, yiannis.pontikes@kuleuven.be, sonja.schreurs@uhasselt.be, wouter.schroeyers@uhasselt.be

Journal: Construction and Building Materials

Abstract

The effect of phosphogypsum (PG) in alkali-activated ground granulated blast furnace slag (GGBFS) on the reactivity, strength development and final matrix properties was investigated, as a function of alkali activator. The results were compared with alkali-activated reference samples from GGBFS. PG completely dissolves and takes part in solid reaction product formation. Upon PG incorporation, portlandite and ettringite are initially formed after dissolution. The hardened binder consists mainly of amorphous hydration products, intermixed with thenardite and minor amounts of secondary gypsum and merwinite. PG incorporation resulted in faster initial and delayed final setting time, while it enhanced the compressive strength and amorphous phase development when sodium hydroxide was used. PG gave rise to a decrease of Al/Si and Ca/Si ratios in the C-A-S-H gels and a higher polymerized network.

Keywords

Super-sulphated cement, alkali-activated binder, ground granulated blast furnace slag, phosphogypsum, hydration, building material

1. Introduction

The search for new binders, wherein Ordinary Portland Cement (OPC) gets partly or totally replaced by other resources, can contribute to the reduction of energy usage and carbon dioxide generation caused by OPC's manufacture. Super-sulphated cements (SSC) are alternative binders which are free (or almost free) of OPC, and consist in most cases of 70-90% ground granulated blast furnace slag (GGBFS), 10-20% gypsum and an alkali activator [1–3]. Next to their environmental benefits [4,5], SSC show promising potential for industrial applications because of their technical performance, e.g. high strength [6] and excellent resistance to chemically aggressive surroundings [1,3,7].

Considering the availability of various gypsum-rich waste streams, there is a strong interest in finding applications that could in effect be both economically viable and sustainable. In this respect, phosphogypsum (PG) forms a potential candidate as gypsum source in the synthesis of SSC. PG is a by-product originating from the production process of phosphoric acid, consisting mainly of $CaSO_4.2H_2O$ and impurities, such as fluoride, remnants of phosphoric acid, heavy metals (e.g. Cd or Cr) and naturally occurring radionuclides (mainly from the ^{238}U decay chain). Worldwide, large quantities are disposed in ponds or heaps without purification, because existing purification techniques are not effective [8,9] and this practice may increase the costs [10]. For this reason, PG has very low recycling rates and it is predicted that the total amount disposed will range from 7 to 8 billion tons by 2025 [11], requiring large disposal areas and necessitating proper management to avoid environmental pollution. Furthermore, a future increase in production volumes is expected because of increasing food production demand accompanied by increasing fertilizer production [9,11,12]. Because of these large volumes, the construction industry is considered to form a possible valorization route. However, if PG is considered for reuse in building applications, the maximum level of naturally occurring radionuclides in building materials is being regulated by the European Basic Safety Standards (EU-BSS) [13], provoking limitations. Therefore, this work is complementary to a previous investigation that deals with the radiological impact of the same binders [14], where it was concluded that maximum 10 wt% PG could be incorporated in order to produce innovative, environmental-safe building materials, which integrate industrial by-products yet comply with existing safety standards.

Slags from iron and steel manufacture, such as GGBFS and ladle slag, respectively, can even react with gypsum without an activator, due to their alkalinity (i.e. high CaO + MgO content) [1]. Despite, fluoride and remnants of phosphoric acid in PG decline the reaction rate and consequently increase the setting time [9]. To achieve a sufficient reactivity, an alkaline surrounding is preferable, provided by an alkaline solution in this investigation.

SSC from GGBFS, PG and an alkali activator could form a new class of alternative sustainable binders, by avoiding the use of OPC and creating a valorization route for PG. However, due to its impurities, the effect of PG incorporation on the reactivity, strength development and final matrix properties should be investigated, which forms the purpose of this study. Also, the use of different alkali activators is investigated. Reactivity is assessed by recording the setting time of the pastes, while isothermal calorimetry and in-situ X-ray diffraction (XRD) analysis were employed to monitor the reaction rate of the product formation. Final matrix properties were investigated by measuring compressive strength and applying micro-chemical analysis. Fourier-transformed infrared (FTIR) spectroscopy and XRD were used for investigation of the hydration products.

2. Materials and methods

2.1 Precursors

GGBFS was derived from iron extraction in a Belgian steel producing company. PG originated from a PG processing plant in Gdansk (Poland) and was provided by the International Atomic Energy Agency (IAEA) (reference material n° 434) [15]. After deriving, GGBFS was dried at 110 °C for 24 h and milled to a Blaine value of 4050 ± 200 cm^2/g, calculated according to EN 196-6 [16]. The density of GGBFS was measured with a Quantachrome Multipycnometer (MPV-6DC) and found to be 2.9 g/cm^3, according to ASTM C204 [17]. The chemical composition of GGBFS was analyzed by X-ray fluorescence analysis (XRF) using a Philips PW 1830 instrument, and is summarized in Table 1. PG was used as received with a d_{50} value of around 3 μm and the matrix composition was (in wt%): 96.0 $CaSO_4.2H_2O$, 1-2 P_2O_5, 1.2 F^-, 1.0 SiO_2 and 0.2 Al_2O_3 [15]. FTIR spectroscopy (Bruker Vertex 70) was performed on GGBFS, PG and a GGBFS/PG mixture by proportion of 9/1 (which is the applied precursor weight ratio, see Table 2). Spectra were acquired from 4000 cm^{-1} to 450 cm^{-1}, at a resolution of 4 cm^{-1} and with 32 scans per measurement, supported by Opus software. Prior to measurement, a background spectrum was recorded. XRD measurements were performed on GGBFS

and PG. They were milled for 5 min in a McCrone micronizing mill with corundum grinding elements and ethanol to obtain accurate fineness. As an internal standard material, 10 wt% of analytical-grade crystalline ZnO (purity 99.9%, Merck) was added. An automated diffractometer with Cu-Kα-radiation (D2 PHASER, Bruker) with a Lynx-eye super speed position sensitive detector was applied for the XRD analysis. An anti-scatter slit positioned 3 mm above the sample was used to protect the detector from abundant X-rays at lower 2θ degrees. In order to reduce preferred orientation, the samples were prepared using the back loading technique. The settings for the X-ray tube generator were 30 kV and 10 mA. To improve statistics, the samples were rotated at 15 rpm during the measurement. Diffractograms were recorded in continuous PSD fast mode between 5° and 70° 2θ at 0.02° step size and a counting time of 0.3 s per step. The diffractograms were qualitatively investigated with EVA V.3.1 (Bruker AXS). Quantitative analysis was performed with MAUD [18] based on the Rietveld method [19–21]. From the known initial ZnO content of 10 wt%, the crystalline and amorphous phase contents were recalculated.

Table 1: Chemical composition of GGBFS

Chemical compound	Wt%
SiO_2	36.2 ± 0.2
CaO	40.3 ± 0.5
Al_2O_3	11.4 ± 0.2
MgO	8.2 ± 0.1
SO_3	1.1 ± 0.1
TiO_2	0.8 ± 0.1
Na_2O	0.8 ± 0.1
K_2O	0.5 ± 0.1
Fe_2O_3	0.3 ± 0.1

2.2 Sample's mix design

To investigate the effects of PG incorporation, six mixtures were designed. The alkali activators used were the combination of a sodium silicate solution (molar ratio SiO_2/Na_2O = 3.3 and 65% water, supplied by ABCR GmbH), sodium hydroxide pellets (grade 99%, supplied by Chem-Lab) and distilled water (ASTM type II), and were prepared one day prior to sample synthesis. The mix designs are

summarized in Table 2. The mixing time amounted 3 min. An alkali activator/precursor ratio of 0.6 was chosen because a decline in the workability was observed upon PG incorporation, caused by its high specific surface area. This ratio was retained for the synthesis of pure GGBFS samples for the sake of comparison.

Table 2: Sample's mix design (partly adapted from [14])

Sample	wt% GGBFS	wt% PG	Alkali activator/Precursor	SiO_2/Na_2O	H_2O/Na_2O
SS1	90	10	0.6	0.75	20.0
SH2	90	10	0.6	0	27.8
SH3	90	10	0.6	0	18.5
SS4	100	0	0.6	0.75	20.0
SH5	100	0	0.6	0	27.8
SH6	100	0	0.6	0	18.5

2.3 Physico-chemical analysis

Isothermal calorimetry was executed at 20 °C using a TAM-Air Isothermal Calorimeter (TA Instruments). First the precursor was inserted in the admix ampoule and the alkali activator into the syringe. Then the ampoule was added into the calorimeter and once thermal equilibrium was obtained, precursors and alkali activators were mixed for 3 min prior to measurement. For determination of the setting time, pastes were prepared and loaded in a Vicat apparatus (Matest E044N Vicatronic) in accordance with EN 196-3 [22]. For selected samples, in-situ XRD (D2 PHASER (Bruker)) was applied. The surface of the paste was smoothed and the sample holder was sealed with Kapton film to prevent water loss and carbonation. The hydrating paste was measured for 22 h and diffractograms between 6° and 55° 2θ were assembled at time intervals of 13 min and with a step-size of 0.02° 2θ and counting time of 0.3 s per step. An anti-scatter slit was positioned 1 mm above the sample. The settings for the X-ray tube generator were 30 kV and 10 mA. The temperature inside the diffractometer case was 20 °C during the measurements. The diffractograms were qualitatively investigated with EVA V.3.1 (Bruker AXS). For compressive strength tests, fresh paste mixes were cast in polymer coated steel molds (20 mm x 20 mm x 80 mm), wrapped in plastic foil to prevent drying

and cured at 20 °C. The samples were demolded after 24 h and further cured at 20 °C in sealed vessels. After 7 and 28 days, five specimens of each formulation were tested with an Instron 5985 machine equipped with a 250 kN load cell. Quantitative elemental point analysis was performed after 28 days of curing with electron probe micro-analysis (EPMA) (Jeol JXA-8530F (FEG)). Specimens sampled from the middle of the cured samples were embedded in epoxy resin, polished and coated with a 25 nm C layer. The settings for the microprobe were 15 kV and 15 nA. The standards of obsidian (for Al, Na and Si), apatite (for Ca and P), celestite (for S), pyrite (for Fe), periclase (for Mg) and kaersutite (for K) were used. Also the background was measured under these conditions. Mappings for Al, Ca, Mg, Na, S and Si were obtained with a dwell time of 40 ms per pixel in a mapped area of 480 x 345 µm (pixel size 1 µm). FTIR spectroscopy was performed after 28 days of curing. After their curing period, samples were dried at 40 °C till constant weight and subsequently crushed in a porcelain mortar and passed through a 45 µm sieve. Measurements were carried out with the same procedure as described earlier (section 2.1). XRD measurements were performed after 28 days of curing. After their curing period, samples were dried at 40 °C in a laboratory oven till constant weight whereafter they were grinded in a porcelain mortar. Subsequent milling, measurements and analyses were performed as explained in section 2.1.

3. Results and discussion

3.1 Isothermal calorimetry and setting time

Fig. 1 shows the heat evolution curves, calculated based on total sample mass (precursor + alkali activator). Time zero represents the time after 3 min of mixing.

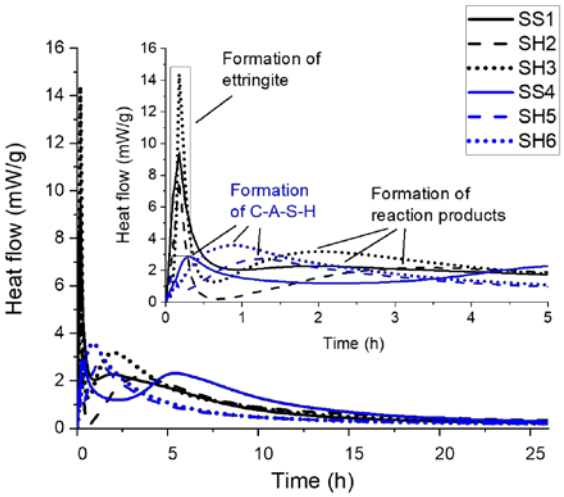

154

155 **Figure 1**: Heat flow

156 As GGBFS is used as precursor, the main reaction product formed upon alkali activation is expected
157 to be a calcium aluminosilicate hydrate (C-A-S-H) type gel [23], which is different from the calcium
158 silicate hydrate (C-S-H) generated in OPC hydration. Generally, C-A-S-H could be viewed as a C-S-H
159 wherein Al^{3+} is located within the silicate chains, more specifically at the tetrahedral bridging sites
160 [23,24]. The incorporation of 10 wt% PG forms a source of Ca^{2+} and SO_4^{2-} ions enhancing the
161 formation of secondary reaction products. The rate of reaction product formation is inherently
162 determined by various parameters, and consequently these reactions can occur simultaneously or in
163 sequence. The heat flow curves can be interpreted as the summation of heat released and consumed
164 by these reactions. For samples SS1, SH2 and SH3, an initial very intense peak with short duration
165 (from approximately 0.1 to 0.5 h) is observed, which corresponds to the formation of ettringite
166 (confirmed by in-situ XRD, section 3.3), being a hexacalcium aluminate trisulphate hydrate mineral,
167 with as chemical formula $Ca_6Al_2(SO_4)_3(OH)_{12}.26H_2O$ [25]. In cement hydration, it was also found that
168 ettringite immediately forms after dissolution [26]. During its formation, crystalline water and a
169 framework of hydrogen bonds are formed upon consuming water from the alkali activator. After this,
170 a dormant period is observed, meaning that the formation of other reaction products is postponed,
171 most likely because of a reduced amount of water available for reactions and surface blockage of
172 GGBFS grains by ettringite, which initially hindered their further hydration. The onset of the peak of

reaction product formation is therefore shifted to later time and this peak is much broader as for pure GGBFS samples, indicating a slower reaction rate as a consequence of fluoride and remnants of phosphoric acid in PG. The presence of silicates in the alkali activator, and a lower H_2O/Na_2O for sodium hydroxide alkali activators, causes a shift of the peak of reaction product formation to earlier times. The height of both the peak of ettringite formation (9.4 mW/g, 7.7 mW/g and 14.4 mW/g after 0.2 h for sample SS1, SH2 and SH3, respectively) and the peak during reaction product formation (2.3 mW/g at 1.8 h for SS1, 2.2 mW/g at 3.4 h for SH2 and 3.2 mW/g at 2 h for SH3) is inversely proportional to the H_2O/Na_2O ratio of the alkali activator. The heat release during reaction product formation is comparable with values found in literature on SSC [1].

The curve shape of pure GGBFS-based binders are similar to data published elsewhere [27–29]. For sample SH5, a dissolution peak is observed at first, whereafter a dormant period follows. Subsequently, a broader exothermic peak is recorded. During the dissolution and the dormant period, the concentration of dissolved species gradually increases, whereupon C-A-S-H formation starts when concentrations reach a threshold [30,31]. For samples SS4 and SH6, there is no dormant period, indicating that immediately after dissolution the concentration threshold was reached to start C-A-S-H formation. The height of the peak during C-A-S-H formation is inversely proportional to the H_2O/Na_2O of the alkali activator. Sample SS4 is characterized by a maximum heat flow of 2.9 mW/g after 0.3 h, for sample SH5 this was 2.7 mW/g after 1.2 h and for sample SH6 3.6 mW/g after 0.9 h. The presence of silicates in the alkali activator accelerates C-A-S-H formation, and a decrease of H_2O/Na_2O for sodium hydroxide alkali activators results in a shift of the peak to earlier time. For sample SS4, another broad peak after 5 h is observed, likely representing further densification of the C-A-S-H structure.

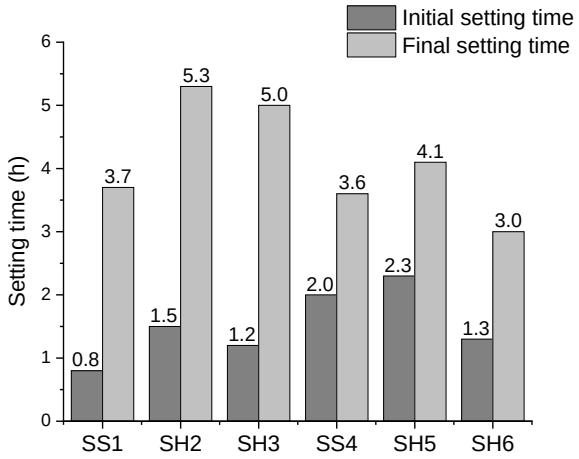

195

196 **Figure 2**: Setting time

197 These thermal characteristics can be correlated to the initial and final setting times of the paste
198 samples, which are presented in Fig. 2. Time zero represents 3 min after the start of mixing. In
199 general, the incorporation of 10 wt% PG results in a faster initial setting (due to the high specific
200 surface area of PG and early ettringite formation) (i.e. a reduction of 0.1 h to 1.2 h) but slower final
201 setting (due to (1) a reduced amount of water available for the reactions, (2) initial surface coverage
202 of GGBFS grains by ettringite and (3) fluoride and remnants of phosphoric acid acting as set retarder
203 [32]) (i.e. an increase of 0.1 h to 2 h). The alkali activator with the highest H_2O/Na_2O (i.e. samples SH2
204 and SH5), led to highest initial and final setting times. The type and concentration of alkali activator
205 plays an essential role in order to control the setting times, which is already extensively reported in
206 literature on alkali-activated slags [33–35] confirming the results for samples SS4, SH5 and SH6.
207 Regarding the initial setting times, samples SS1, SH2 and SH3 fulfill the requirements defined in EN
208 15743 [2] on SSC (initial setting time ≥ 0.75 h), providing an appropriate time in real construction
209 applications.

210

211 **3.2 In-situ XRD**

212 In-situ XRD was performed for sample SH3 which displayed the highest heat flow peak from

approximately 0.1 to 0.5 h in isothermal calorimetry (section 3.1). The results are visualized in Fig. 3.

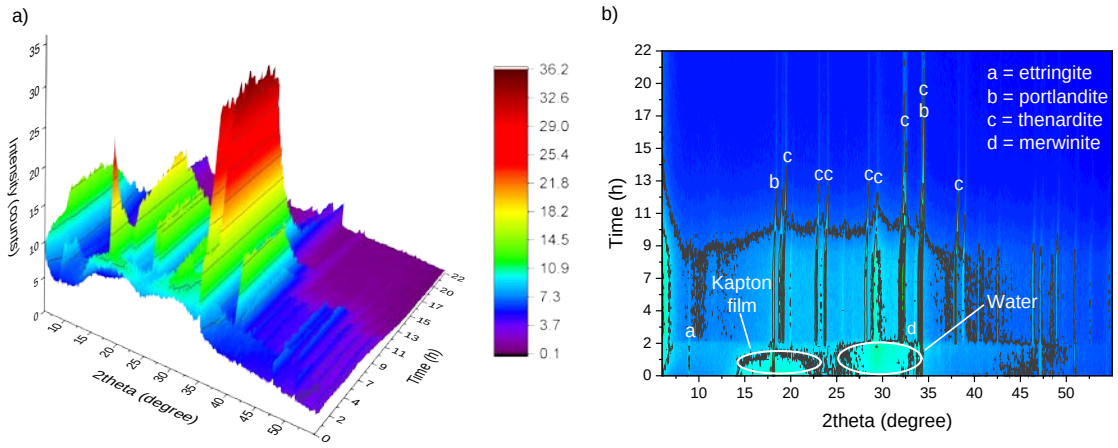

Figure 3: In-situ XRD sample SH3: a) 3D and b) 2D view (top view of Fig. 3a)

The understanding of the individual reactions occurring during the hydration is of fundamental importance to understand and control the final properties. From Fig. 3, it can be seen that the hydration forms a summary of several reactions, depending on the system thermodynamics and hydration kinetics. In general, it can be observed that the existence of X-ray amorphous phases is variable over time, and gradually increases during hardening. No gypsum, anhydrite or bassanite peaks were observed, proving the complete dissolution of PG upon mixing. In other words, a hydraulic binder is created. The phases determined are ettringite, portlandite, thenardite and merwinite, revealing the action of PG on hydration. Immediately after mixing, portlandite is formed, causing a decrease in pH. Following, but still very early in the reaction (from approximately 13 min up to 2.5 h), ettringite is formed, consuming a large amount of water and covering the surface of undissolved GGBFS grains. However, ettringite appears not stable because of the pH decrease upon portlandite formation and decomposes again [36], giving rise to thenardite formation from 2.5 h. Merwinite originates from GGBFS (section 3.6) and was mainly visible in the first 10 scans from the undissolved GGBFS grains covered by ettringite. The formation of thenardite increases the pH because the sulphate concentration drops [37], accelerating GGBFS dissolution. For this reason, merwinite disappears upon thenardite formation. In fact, the system acts like a hybrid system, in

232 which a certain amount of activator is necessary to develop a cascade of formation and dissolution
233 reactions. After about 12 h, the intensity of the peaks of portlandite and thenardite decreases
234 because the amorphous content is increasing. After 22 h, the hardened sample consists of
235 amorphous hydration products, intermixed with thenardite and portlandite. Because thenardite is a
236 salt, leftovers will give rise to high leaching rates of sodium and sulphate when in contact with water.
237 Therefore, ideally all the thenardite gets totally consumed during hydration. Also for samples SS1 and
238 SH2, thenardite was left after 28 days of curing (confirmed by XRD, section 3.6), which is not
239 desirable from the leaching point of view. On the contrary, the formation of thenardite is enviable
240 from the microstructural development point of view, giving rise to enhanced strength (section 3.3)
241 because of accelerated GGBFS dissolution.

242

243 **3.3 Compressive strength testing**

244 Fig. 4 shows the compressive strength (1 sigma) at 7 and 28 days. For all samples, an increase in
245 compressive strength is observed when extending the curing period, attributed to the development
246 of reaction products to different degrees as a function of sample's mix design. Compared with the
247 reference samples, the incorporation of 10 wt% PG for samples SS1, SH2 and SH3 resulted in strength
248 reduction (33.1% at 28 days) for the sodium silicate activated samples (SS1), while it caused a
249 strength gain for sodium hydroxide activated ones (SH2 and SH3) (55.3% and 89.0% at 28 days,
250 respectively). This is likely due to a slightly higher amorphous content (see further in section 3.6) of
251 SH2 and SH3, compared with SH5 and SH6, respectively. The strength reduction for SS1 agrees with a
252 lower amorphous content compared to SS4. Resulting from the presence of additional silicate
253 species, samples activated with sodium silicate (SS1 and SS4) showed significant higher strength
254 compared with sodium hydroxide activated samples, due to enhanced solid product formation and
255 the formation of a higher polymerized structure (see also FTIR, section 3.5). For sodium hydroxide
256 activated samples, an increase in Na_2O concentration (SH3 and SH6) led to an increase in

compressive strength at 28 days (compared to SH2 and SH5, respectively), which can be explained by a higher dissolution rate of precursors, resulting in more species available for reaction product formation. The compressive strength at 28 days of pure GGBFS samples (SS4, SH5 and SH6) is comparable with values found in literature, although the applied alkali activator/precursor ratio of 0.6 is higher than mostly used [38].

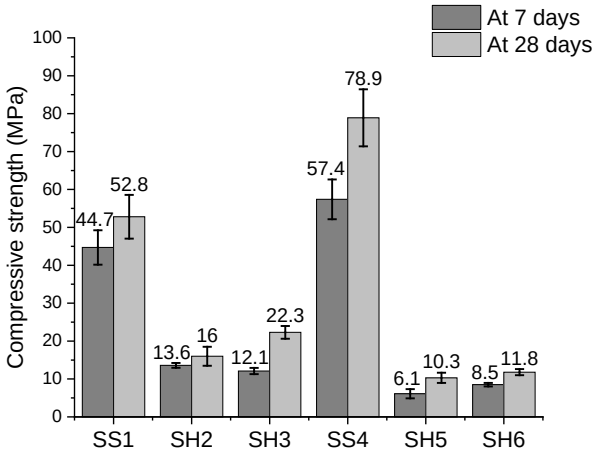

Figure 4: Compressive strength after 7 and 28 days of curing

Only for sample SS1, the compressive strength at 7 and 28 days exceeds the minimum legitimated in the European standard for SSC [2]. Though, depending on the considered application, different strengths are required, e.g. for driveways and footpaths typical compressive strengths are ranging from 15 MPa to 25 MPa, while the strength for structural concrete for bridge deck slabs should achieve 32 MPa. The compressive strength of superstructures ranges from 40 MPa to 50 MPa and concrete pavements require 30 MPa [39]. Nonetheless, this is merely the first data and additional testing at later ages, accelerated testing and repeating these tests on concrete samples is needed in order to safely define proper applications.

3.4 Micro-chemical analysis

Micro-chemical analysis was performed after 28 days of curing and backscattered electron (BSE) images (500 times magnification) are shown in Fig. 5. The samples demonstrate a heterogeneous microstructure, consisting of a mix of solid reaction products (darkest areas) and undissolved GGBFS particles (lightest areas). Upon PG incorporation, different reaction products are formed (indicated by R1 and R2 in Fig. 5). R1 represents the C-A-S-H gel, while R2 could indicate secondary gypsum, thenardite and/or monosulphate (see further in section 3.6). Microcracks presumably have developed during sample preparation (when they are placed in vacuum for coating).

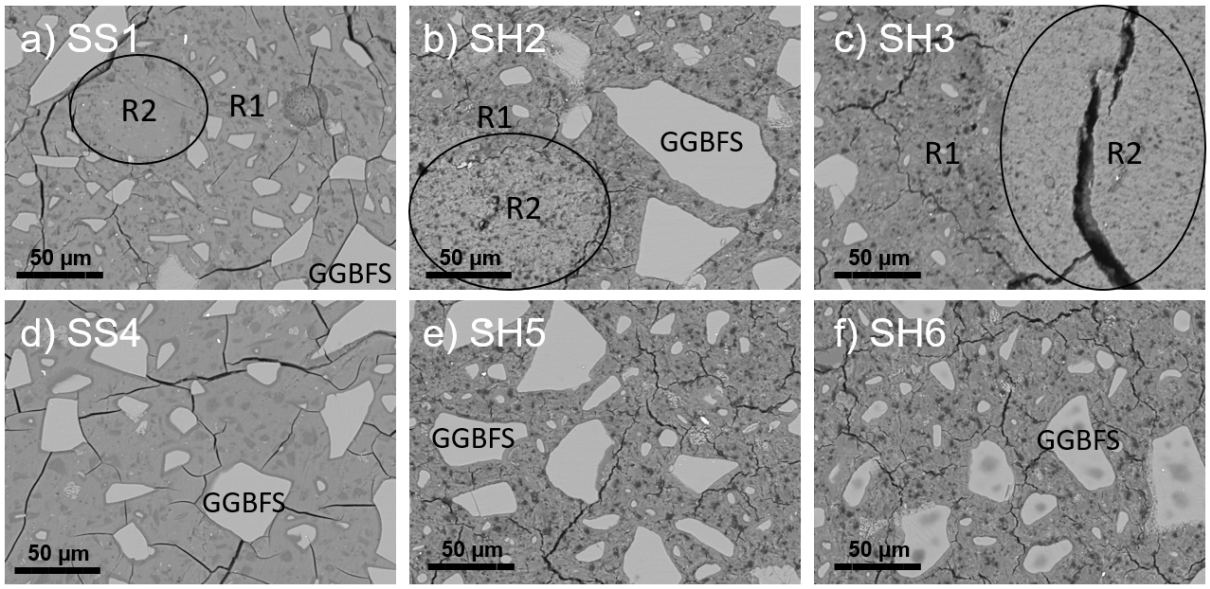

Figure 5: BSE images after 28 days of curing: a) SS1, b) SH2, c) SH3, d) SS4, e) SH5 and f) SH6

Quantitative elemental point analysis was performed, the results are not presented due to unacceptable high uncertainties. It is not always straightforward to understand what is located underneath the sample surface since the excited volume for such analysis lies in the micrometer range, which is considerably large to elucidate a whole of intermixed solid hydration products. For this reason, mappings are more reliable, which are shown in Fig. 6 for samples incorporated with PG. Undissolved GGBFS particles are embedded in the C-A-S-H gel, while regions of secondary gypsum (SG, see further in section 3.6) and thenardite (T) are clearly detectable.

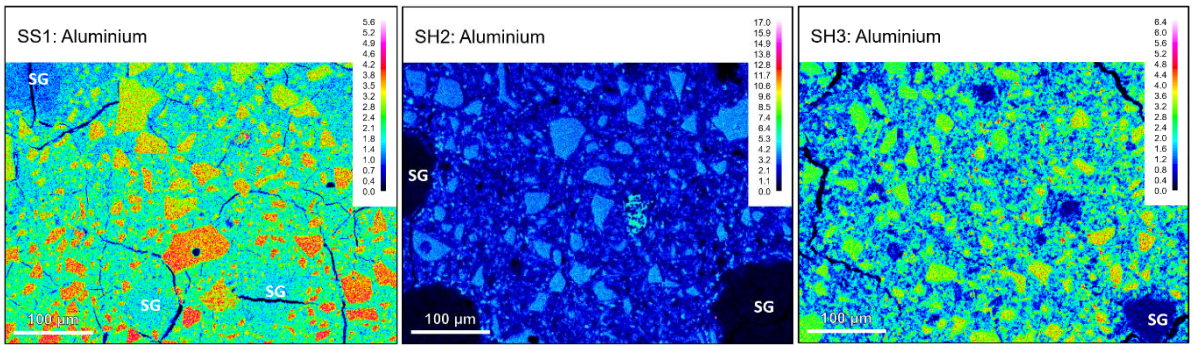

290

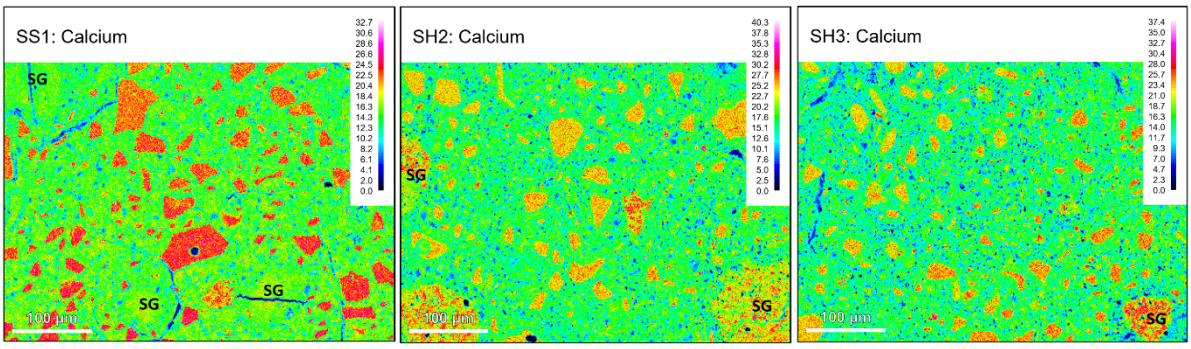

291

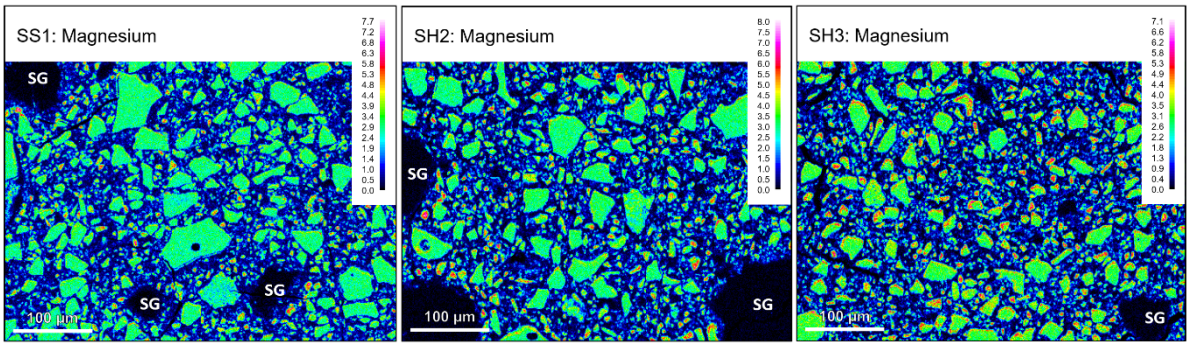

292

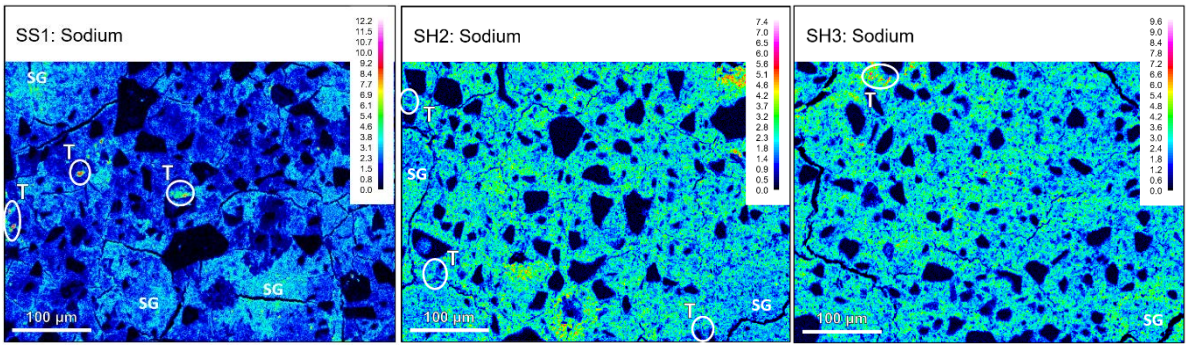

293

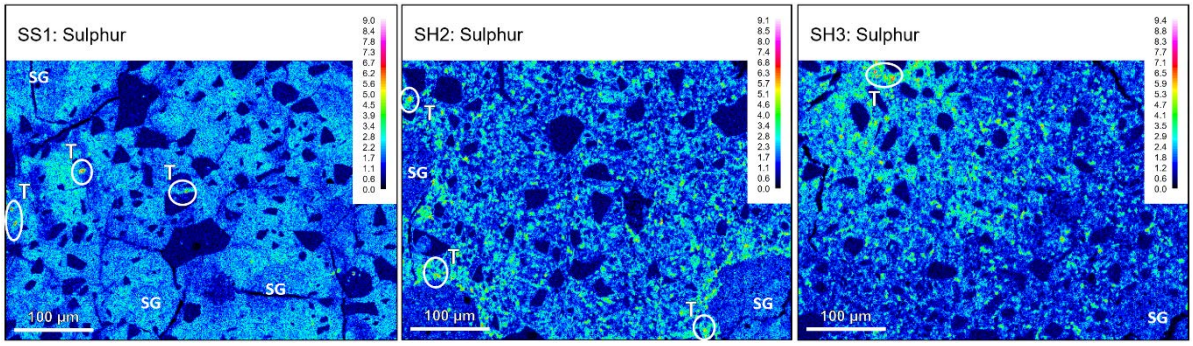

294

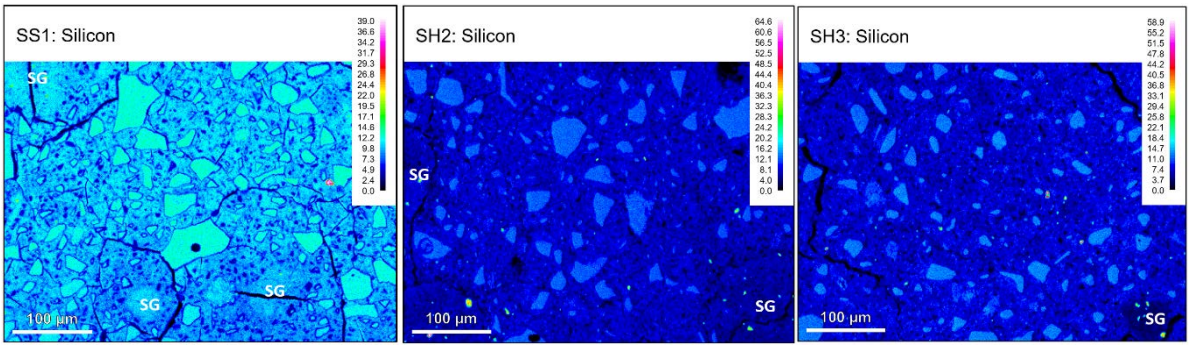

Figure 6: Mappings of samples SS1, SH2 and SH3 after 28 days of curing

3.5 Fourier-transform infrared

FTIR spectra of the precursors (Fig. 7a) were recorded to visualize the change in the spectrum when precursors get alkali-activated. For the sake of clarity, spectra were shifted upwards and have been plotted from 3800 to 450 cm^{-1}. GGBFS presented a stretching vibration (Si-O bonding) centred at around 890 cm^{-1}. The broadness of the stretching vibration of the GGBFS/PG mixture, centred at around 900 cm^{-1}, was larger than those for GGBFS, which is the reference to observe the hydration process. For PG, the bands centred at 1105, 1090, 1005, 659 and 595 cm^{-1} are assigned to the stretching and bending modes of sulphate. The bands at 1105 and 1090 cm^{-1} correspond to the asymmetrical v_3 vibrations, the band at 1005 cm^{-1} corresponds to the asymmetrical v_1 vibrations, and the ones at 659 and 595 cm^{-1} to the asymmetrical v_4 vibrations [40]. The stretching vibration of the H_2O molecules occurs at 3600, 3560 and 1616 cm^{-1}. The bands at 675, 614 and 595 cm^{-1} are characteristic for anhydrite [41], indicating that some amount of $CaSO_4.2H_2O$ was transformed to $CaSO_4.0.5H_2O$ and $CaSO_4$ (confirmed by XRD, section 3.6).

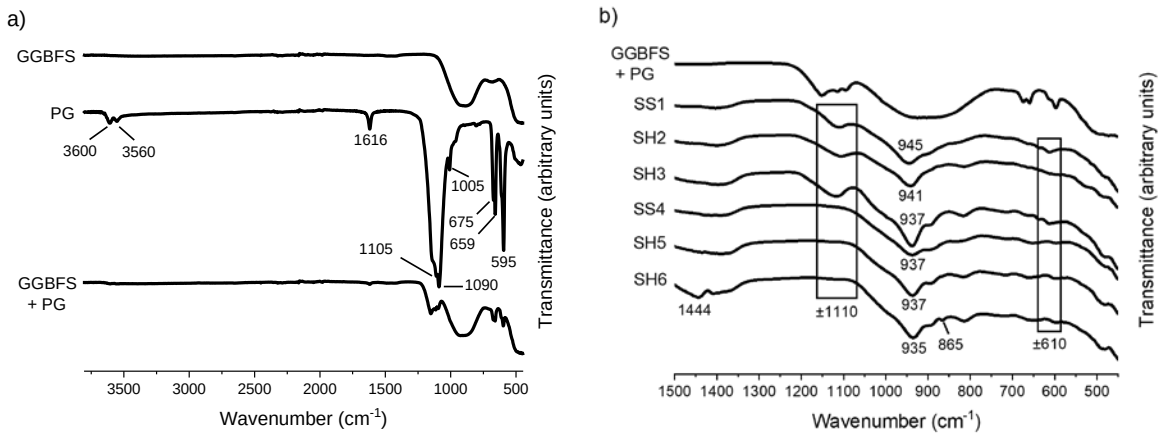

311

312 **Figure 7**: FTIR spectra of a) precursors and b) samples after 28 days of curing

313 As a result of the amorphous character of alkali-activated binders, disabling the applicability of XRD
314 for characterization of the non-crystalline phases, FTIR spectroscopy was applied to gain useful
315 information. Fig. 7b shows the FTIR spectra of samples at 28 days. Since there were no major
316 changes within the 4000 to 1500 cm^{-1} region, data were plotted from 1500 to 450 cm^{-1} and the
317 spectra were shifted upwards. Because GGBFS was used as precursor, the formation of C-A-S-H gel as
318 main reaction product is expected [28,42–44]. The stretching vibration of Si-O-T (T stands for Al or Si)
319 units (generated by Q^2 units), commonly observed around 940 cm^{-1} upon alkali activation [45–47],
320 provides valuable information about the constitution of reaction products. This stretching vibration is
321 related to a low-polymerized silicate network, wherein Si gets partly substituted by other elements
322 (e.g. Al), and where non-bridging oxygens (e.g. Si-O-Na) occur [48,49]. Other bands, which are also
323 characteristic for the Si-O-T units, are the ones around 400-500 cm^{-1} (deformation vibrations) and
324 around 700-800 cm^{-1} (typical for Q^1 units) [50]. No Q^3 units were discovered (i.e. at 1200 cm^{-1}). The
325 broader these Si-O-T bands, the more amorphous the material, while an increase in their
326 wavenumber designates a more polymerized network (enhanced Si content in the C-A-S-H gel). From
327 Fig. 7b, it can be seen that the strongest bands lay in the interval of 930-950 cm^{-1}, and as stated
328 earlier, being the stretching vibration area for C-A-S-H gels from GGBFS activation [51]. The changes
329 located at the stretching vibration area for samples incorporated with 10 wt% PG (SS1, SH2 and SH3)
330 to slightly higher wavenumbers, could be attributed to the decrease of Al/Si and Ca/Si ratios in the

gels [52] and a higher polymerization network. On the contrary, sample SS4, activated with a sodium silicate solution, did not possess a change of the stretching vibration band to higher wavenumbers, compared with sodium hydroxide activated ones (SH5 and SH6). An explanation for this behavior could be that in spite of the fact that a higher polymerized structure was formed when using a sodium silicate solution, the intensity of the absorption was diminished due to their slightly higher amorphous nature (broader band), whereby the resulting peak was not shifted to higher energies. On the other hand, this could also indicate that changing the SiO_2/Na_2O molar ratios of the alkali activator has minor influence on the degree of polymerization. However, the first suggestion is assumed to be more realistic regarding compressive strength (section 3.3) and confirmed by Q-XRD (section 3.6). The stretching vibration band, and the ones located around 400-500 cm^{-1} and 700-800 cm^{-1}, show highest intensity for samples SH3 and SH6, most likely caused by an initially higher precursor dissolution rate due to a higher Na_2O content in the alkali activator. The band around 800 cm^{-1} is less clear for samples activated with sodium silicate (SS1 and SS4), which is commonly observed for silicates with high network modifiers [50]. All samples displayed OH^- groups at around 1650 cm^{-1} and 3600 cm^{-1} (not presented in the figure), indicating the occurrence of chemically bound water across the reaction products [53]. For sample SH6, carbonation has taken place, deduced from the bands at 865 cm^{-1} and 1444 cm^{-1}, which are related to the asymmetric stretching vibration of O-C-O bonds [54,55]. Since carbonation was not observed for SH3, this phenomenon could be impeded by the incorporation of PG. The band observed at 1400 cm^{-1} for all samples might indicate the presence of hydroxyl groups in the material. The bands in the region from 500 to 700 cm^{-1} may be characteristic for iron-containing phases [56], but are in this case more probably caused by the Al-O bonding. The bands at 1110 cm^{-1} and 610 cm^{-1} for samples SS1, SH2 and SH3 are nonexistent in the spectra of alkali-activated binders containing exclusively GGBFS, and correspond to thenardite, secondary gypsum and/or monosulphate (see further in section 3.6). The band at 1110 cm^{-1} represents the asymmetric stretching vibration of SO_4^{2-}, while the band at 610 cm^{-1} corresponds to its out-of-plane bending vibration [57,58].

3.6 XRD

Fig. 8a shows the diffractograms of the precursors. The asterisks indicate the peaks from the internal ZnO standard. GGBFS was predominantly amorphous with a trace of merwinite ($Ca_3Mg(SiO_4)_2$, 5.3 wt%). PG comprised a mixture of 33.2 wt% $CaSO_4.2H_2O$, 27.1 wt% $CaSO_4.0.5H_2O$, 32.1 wt% $CaSO_4$ (also confirmed by FTIR, section 3.5) and 7.6 wt% amorphous phases.

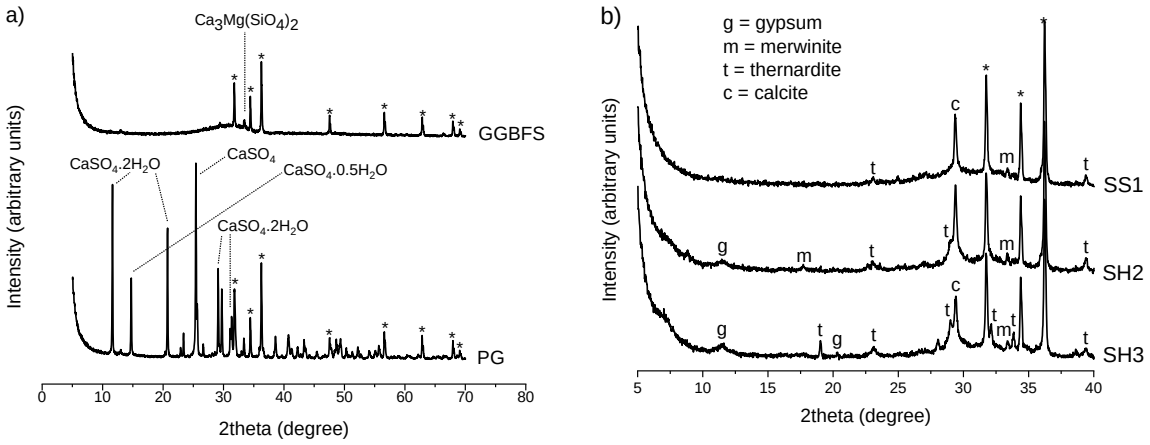

Figure 8: XRD patterns of a) precursors and b) samples incorporated with PG after 28 days of curing

As a result of the highly amorphous character of alkali-activated binders, only little information about the crystalline phases could be gained from their diffractograms after 28 days of curing (shown in Fig. 8b for samples incorporated with PG). The data were plotted from 5 to 40 2θ, the peaks from the internal ZnO standard are marked with an asterisk. Peaks of gypsum, merwinite, thenardite and calcite were detected. Carbonation (formation of calcite) had occurred during sample preparation (wet milling with ethanol and subsequent evaporation), since it was not observed in their FTIR spectra (section 3.5). Peaks of gypsum were not observed with in-situ XRD during the first 22 h. However, the conversion of early ettringite results in the presence of secondary gypsum and monosulphate ($Ca_4Al_2SO_4(OH)_{12}.6H_2O$) according to Eq. 1 [37]:

$$Ca_6Al_2(SO_4)_3(OH)_{12}.26H_2O \rightarrow Ca_4Al_2SO_4(OH)_{12}.6H_2O + 2\,CaSO_4 2H_2O + 16\,H_2O \quad (Eq.1)$$

Despite, monosulphate is a poorly crystalline phase and hard to detect by XRD [59–61]. Portlandite completely dissapeared after 28 days of curing.

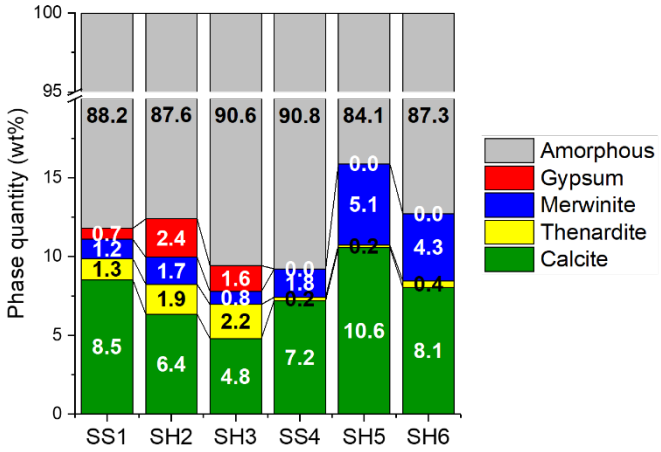

Figure 9: Q-XRD of samples after 28 days of curing

In Fig. 9, the quantitative analysis of X-ray data is presented. From these data it is concluded that the main reaction product was an amorphous C-A-S-H gel for all samples. The amorphous content of sample SS1 was lower compared with SS4, while samples SH2 and SH3 showed increased amorphous content compared to SH5 and SH6, respectively. When comparing Fig. 4 with Fig. 9, it is likely that the amorphous phases are responsible for the compressive strength. The incorporation of PG gave rise to thenardite formation, which increased the GGBFS dissolution and consequently the merwinite content after 28 days was lower compared to the reference samples. Secondary gypsum is present for SS1, SH2 and SH3 upon the dissolution of early ettringite, however does not impede a negative influence on the compressive strength after 28 days. Nonetheless, compressive strength testing and phase development after prolonged curing times should be the subject of further investigation.

4. Conclusions

In this study, the effect of PG incorporation in alkali-activated GGBFS on the reactivity, strength development and final matrix properties was investigated, as a function of alkali activator. The results were compared with alkali-activated reference samples based on GGBFS. PG completely dissolved and took part in solid reaction product formation; a hydraulic binder was created. Upon PG incorporation, portlandite and ettringite were formed immediately after dissolution of precursors. The hardened binder consisted mainly of amorphous hydration products, intermixed with thenardite and minor amounts of secondary gypsum and undissolved merwinite. The formation of thenardite was enviable from the microstructural development point of view, giving rise to accelerated GGBFS dissolution. However, leftovers of thenardite may result in high leaching rates of sodium and sulphate when in contact with water. PG incorporation resulted in faster initial setting (i.e. a reduction of 0.1 h to 1.2 h) and delayed final setting time (i.e. an increase of 0.1 h to 2 h), compared with the reference samples. The incorporation of PG enhanced the compressive strength with 55.3% to 89.0% at 28 days when sodium hydroxide was used as alkali activator, likely due to an increase in the amorphous content. Both the compressive strength and amorphous content were reduced when incorporating PG in sodium silicate activated samples. Regions of secondary gypsum and thenardite were clearly detectable in micro-chemical analysis. An amorphous C-A-S-H type gel was the prevalent reaction product and the incorporation of PG gave rise to a decrease of Al/Si and Ca/Si ratios in the C-A-S-H gels and a higher polymerized network.

Acknowledgements

This work was supported by the fund for scientific research Flanders (FWO) hosted by the University of Hasselt and the University of Leuven. The authors would like to acknowledge the networking support of the COST Action TU1301, www.norm4building.org.

References

[1] A. Gruskovnjak, B. Lothenbach, F. Winnefeld, R. Figi, S.C. Ko, M. Adler, U. Mäder, Hydration mechanisms of super sulphated slag cement, Cem. Concr. Res. 38 (2008) 983–992. doi:10.1016/j.cemconres.2008.03.004.

[2] European Committee for Standardization, EN 15743: Supersulfated cement - composition, specification and conformity criteria, (2010).

[3] M.C.G. Juenger, F. Winnefeld, J.L. Provis, J.H. Ideker, Advances in alternative cementitious binders, Cem. Concr. Res. 41 (2011) 1232–1243. doi:10.1016/j.cemconres.2010.11.012.

[4] E. Gartner, Industrially interesting approaches to "low-CO2" cements, Cem. Concr. Res. 34 (2004) 1489–1498. doi:10.1016/j.cemconres.2004.01.021.

[5] B. O'Rourke, C. McNally, M.G. Richardson, Development of calcium sulfate-ggbs-Portland cement binders, Constr. Build. Mater. 23 (2009) 340–346. doi:10.1016/j.conbuildmat.2007.11.016.

[6] S. Rubert, C.A. Luz, M.V.F. Varela, J.I.P. Filho, R.D. Hooton, Hydration mechanisms of supersulfated cement: The role of alkali activator and calcium sulfate content, J. Therm. Anal. Calorim. 134 (2018) 971–980. doi:10.1007/s10973-018-7243-6.

[7] T. Grounds, D. V Nowell, F.W. Wilburn, Resistance of supersulfated cement to strong sulfate solutions, Jounrla Therm. Anal. Calorim. 72 (2003) 181–190. doi:https://doi.org/10.1023/A:1023928021602.

[8] K. Kovler, M. Somin, Producing environment-conscious building materials from contaminated phosphogypsum, in: N. Kashino, Y. Ohama (Eds.), Int. RILEM Symp. Environ. Mater. Syst. Sustain. Dev., RILEM Publications S.A.R.L., Koriyama, Japan, 2004: pp. 245–253. doi:10.1617/2912143640.029.

[9] A.M. Rashad, Phosphogypsum as a construction material, J. Clean. Prod. 166 (2017) 732–743. doi:10.1016/j.jclepro.2017.08.049.

[10] L. Reijnders, Cleaner phosphogypsum, coal combustion ashes and waste incineration ashes for application in building materials: A review, Build. Environ. 42 (2007) 1036–1042. doi:10.1016/j.buildenv.2005.09.016.

[11] International Atomic Energy Agency (IAEA), Radiation Protection and Management of NORM Residues in the Phosphate Industry, Safety Reports Series No. 78, IAEA, Vienna, 2013. doi:10.1016/j.resourpol.2012.04.002.

[12] J. Hilton, Towards a management and regulatory strategy for phosphoric acid and phosphogypsum as co-products, in: W.C. Gerken (Ed.), Proc. Fifth Int. Symp. Nat. Occur. Radioact. Mater. (NORM V), IAEA, Seville, Spain, 2007: pp. 281–295. doi:10.1016/j.jenvrad.2005.09.006.

[13] Council of the European Union, Council directive 2013/59/EURATOM, European Basic Safety Standards (BSS) for Protection against Ionising Radiation, Off. J. Eur. Union. L 13/1 (2014).

[14] K. Gijbels, R. Ion Iacobescu, Y. Pontikes, N. Vandevenne, S. Schreurs, W. Schroeyers, Radon immobilization potential of alkali-activated materials containing ground granulated blast furnace slag and phosphogypsum, Constr. Build. Mater. 184 (2018) 68–75. doi:10.1016/j.conbuildmat.2018.06.162.

[15] A. Shakhashiro, U. Sansone, H. Wershofen, A. Bollhöfer, C.K. Kim, C.S. Kim, G. Kis-Benedek, M. Korun, M. Moune, S.H. Lee, S. Tarjan, M.S. Al-Masri, The new IAEA reference material: IAEA-434 technologically enhanced naturally occurring radioactive materials (TENORM) in phosphogypsum, Appl. Radiat. Isot. 69 (2011) 231–236. doi:10.1016/j.apradiso.2010.09.002.

[16] European Committee for Standardization, EN 196-6: Methods of testing cement - Part 6: Determination of fineness, (2010).

[17] ASTM International, ASTM C204-17. Standard test methods for fineness of hydraulic cement by air-permeability apparatus, (2017).

[18] L. Lutterotti, S. Matthies, H.R. Wenk, MAUD (Material Analysis Using Diffraction): a user friendly java program for Rietveld texture analysis and more, in: Jerzy A. Szpunar (Ed.), Proc. Twelfth Int. Conf. Textures Mater. / ICOTOM-12, National Research Press, Montreal, 1999: p. 1599.

[19] H.M. Rietveld, A profile refinement method for nuclear and magnetic structures, J. Appl. Crystallogr. 2 (1969) 65–71. doi:10.1107/S0021889869006558.

[20] R.W. Cheary, A.A. Coelho, A fundamental parameter approach to X-ray line-profile fitting, J. Appl. Crystallogr. 25 (1992) 109–121. doi:10.1107/S0021889891010804.

[21] D.L. Bish, S.A. Howard, Quantitative phase analysis using the Rietveld method, J. Appl. Crystallogr. 21 (1988) 86–91. doi:10.1107/S0021889887009415.

[22] European Committee for Standardization, EN 196-3. Methods of testing cement - Part 3: Determination of setting times and soundness, (2016).

[23] J.L. Provis, S.A. Bernal, Geopolymers and related alkali-activated materials, Annu. Rev. Mater. Res. 44 (2014) 299–327. doi:10.1146/annurev-matsci-070813-113515.

[24] F. Puertas, M. Palacios, H. Manzano, J.S. Dolado, A. Rico, J. Rodríguez, A model for the C-A-S-H gel formed in alkali-activated slag cements, J. Eur. Ceram. Soc. 31 (2011) 2043–2056. doi:10.1016/j.jeurceramsoc.2011.04.036.

[25] E. Scholtzová, L. Kucková, J. Kožíšek, D. Tunega, Structural and spectroscopic characterization of ettringite mineral -combined DFT and experimental study, J. Mol. Struct. 1100 (2015) 215–224. doi:10.1016/j.molstruc.2015.06.075.

[26] H.J. Weyer, I. Müller, B. Schmitt, D. Bosbach, A. Putnis, Time-resolved monitoring of cement hydration: Influence of cellulose ethers on hydration kinetics, Nucl. Instruments Methods Phys. Res. Sect. B Beam Interact. with Mater. Atoms. 238 (2005) 102–106. doi:10.1016/j.nimb.2005.06.026.

[27] A. Fernandez-Jimenez, F. Puertas, A. Arteaga, Determination of kinetic equations of alkaline activation of blast furnace slag by means of calorimetric data, J. Therm. Anal. Calorim. 52 (1998) 945–955. doi:10.1023/A:1010172204297.

[28] S. Song, D. Sohn, H.M. Jennings, T.O. Mason, Hydration of alkali-activated ground granulated blast furnace slag, J. Mater. Sci. 35 (2000) 249–257. doi:10.1023/A:1004742027117.

[29] D. Ravikumar, N. Neithalath, Reaction kinetics in sodium silicate powder and liquid activated slag binders evaluated using isothermal calorimetry, Thermochim. Acta. 546 (2012) 32–43. doi:10.1016/j.tca.2012.07.010.

[30] C. Shi, P. V. Krivenko, D. Roy, Alkali-Activated Cements and Concretes, first ed., Taylor & Francis, Oxford, 2006.

[31] S. Chithiraputhiran, N. Neithalath, Isothermal reaction kinetics and temperature dependence of alkali activation of slag, fly ash and their blends, Constr. Build. Mater. 45 (2013) 233–242. doi:10.1016/j.conbuildmat.2013.03.061.

[32] J.H. Potgieter, S.S. Potgieter, R.I. Mccrindle, C.A. Strydom, An investigation into the effect of various chemical and physical treatments of a South African phosphogypsum to render it

503 suitable as a set retarder for cement, Cem. Concr. Res. 33 (2003) 1223–1227.
504 doi:10.1016/S0008-8846(03)00036-X.

505 [33] J.J. Chang, A study on the setting characteristics of sodium silicate-activated slag pastes, Cem.
506 Concr. Res. 33 (2003) 1005–1011. doi:10.1016/S0008-8846(02)01096-7.

507 [34] K.-H. Yang, J.-H. Mun, J.-I. Sim, J.-K. Song, Effect of water content on the properties of
508 lightweight alkali-activated slag concrete, J. Mater. Civ. Eng. 23 (2011) 886–894.
509 doi:10.1061/(ASCE)MT.1943-5533.0000244.

510 [35] B.S. Gebregziabiher, R.J. Thomas, S. Peethamparan, Temperature and activator effect on
511 early-age reaction kinetics of alkali-activated slag binders, Constr. Build. Mater. 113 (2016)
512 783–793. doi:10.1016/j.conbuildmat.2016.03.098.

513 [36] M. Chrysochoou, D. Dermatas, Evaluation of ettringite and hydrocalumite formation for heavy
514 metal immobilization: Literature review and experimental study, J. Hazard. Mater. 136 (2006)
515 20–33. doi:10.1016/j.jhazmat.2005.11.008.

516 [37] F. Winnefeld, B. Lothenbach, Hydration of calcium sulfoaluminate cements - Experimental
517 findings and thermodynamic modelling, Cem. Concr. Res. 40 (2010) 1239–1247.
518 doi:10.1016/j.cemconres.2009.08.014.

519 [38] O. Burciaga-Díaz, J.I. Escalante-García, Structure, mechanisms of reaction, and strength of an
520 alkali-activated blast-furnace slag, J. Am. Ceram. Soc. 96 (2013) 3939–3948.
521 doi:10.1111/jace.12620.

522 [39] International Atomic Energy Agency (IAEA), Guidebook on non-destructive testing of concrete
523 structures, first ed., IAEA, Vienna, 2002.

524 [40] H. Bensalah, M.F. Bekheet, S. Alami Younssi, M. Ouammou, A. Gurlo, Hydrothermal synthesis
525 of nanocrystalline hydroxyapatite from phosphogypsum waste, J. Environ. Chem. Eng. 6
526 (2018) 1347–1352. doi:10.1016/j.jece.2018.01.052.

527 [41] V. Leškevičiene, D. Nizevičiene, Anhydrite binder calcined from phosphogypsum, Ceram. -
528 Silikaty. 54 (2010) 152–159.

529 [42] S.-D. Wang, K.L. Scrivener, Hydration products of alkali activated slag cement, Cem. Concr.
530 Res. 25 (1995) 561–571. doi:10.1016/0008-8846(95)00045-E.

531 [43] C.K. Yip, G.C. Lukey, J.S.J. Van Deventer, The coexistence of geopolymeric gel and calcium
532 silicate hydrate at the early stage of alkaline activation, Cem. Concr. Res. 35 (2005) 1688–
533 1697. doi:10.1016/j.cemconres.2004.10.042.

534 [44] M. Ben Haha, G. Le Saout, F. Winnefeld, B. Lothenbach, Influence of activator type on
535 hydration kinetics, hydrate assemblage and microstructural development of alkali activated
536 blast-furnace slags, Cem. Concr. Res. 41 (2011) 301–310.
537 doi:10.1016/j.cemconres.2010.11.016.

538 [45] I. García-Lodeiro, A. Fernández-Jiménez, M.T. Blanco, A. Palomo, FTIR study of the sol-gel
539 synthesis of cementitious gels: C-S-H and N-A-S-H, J. Sol-Gel Sci. Technol. 45 (2008) 63–72.
540 doi:10.1007/s10971-007-1643-6.

541 [46] S.A. Bernal, R. Mejía De Gutiérrez, A.L. Pedraza, J.L. Provis, E.D. Rodriguez, S. Delvasto, Effect
542 of binder content on the performance of alkali-activated slag concretes, Cem. Concr. Res. 41
543 (2011) 1–8. doi:10.1016/j.cemconres.2010.08.017.

544 [47] I. García Lodeiro, D.E. Macphee, A. Palomo, A. Fernández-Jiménez, Effect of alkalis on fresh C-
545 S-H gels. FTIR analysis, Cem. Concr. Res. 39 (2009) 147–153.
546 doi:10.1016/j.cemconres.2009.01.003.

[48] Z. Zhang, H. Wang, J.L. Provis, F. Bullen, A. Reid, Y. Zhu, Quantitative kinetic and structural analysis of geopolymers. Part 1. the activation of metakaolin with sodium hydroxide, Thermochim. Acta. 539 (2012) 23–33. doi:10.1016/j.tca.2012.03.021.

[49] W.K.W. Lee, J.S.J. Van Deventer, Use of infrared spectroscopy to study geopolymerization of heterogeneous amorphous aluminosilicates, Langmuir. 19 (2003) 8726–8734. doi:10.1021/la026127e.

[50] F. Gervais, A. Blin, D. Massiot, J.P. Coutures, M.H. Chopinet, F. Naudin, Infrared reflectivity spectroscopy of silicate glasses, J. Non. Cryst. Solids. 89 (1987) 384–401. doi:10.1016/S0022-3093(87)80280-6.

[51] I. Ismail, S.A. Bernal, J.L. Provis, R. San Nicolas, S. Hamdan, J.S.J. Van Deventer, Modification of phase evolution in alkali-activated blast furnace slag by the incorporation of fly ash, Cem. Concr. Compos. 45 (2014) 125–135. doi:10.1016/j.cemconcomp.2013.09.006.

[52] D. Ravikumar, N. Neithalath, Effects of activator characteristics on the reaction product formation in slag binders activated using alkali silicate powder and NaOH, Cem. Concr. Compos. 34 (2012) 809–818. doi:10.1016/j.cemconcomp.2012.03.006.

[53] P. Yu, R.J. Kirkpatrick, B. Poe, P.F. McMillan, C. Xiandong, Structure of calcium silicate hydrate (C-S-H): Near-, mid-, and far-infrared spectroscopy, J. Am. Ceram. Soc. 82 (1999) 742–748. doi:10.1111/j.1151-2916.1999.tb01826.x.

[54] M. Yousuf, A. Mollah, T.R. Hess, Y.-N. Tsai, D.L. Cocke, An FTIR and XPS investigations of the effects of carbonation on the solidification/stabilization of cement based systems-Portland type V with zinc, Cem. Concr. Res. 23 (1993) 773–784. doi:10.1016/0008-8846(93)90031-4.

[55] S.A. Bernal, J.L. Provis, V. Rose, R. Mej??a De Gutierrez, Evolution of binder structure in sodium silicate-activated slag-metakaolin blends, Cem. Concr. Compos. 33 (2011) 46–54. doi:10.1016/j.cemconcomp.2010.09.004.

[56] T. Hertel, B. Blanpain, Y. Pontikes, A proposal for a 100 % use of bauxite residue towards inorganic polymer mortar, J. Sustain. Metall. 2 (2016) 394–404. doi:10.1007/s40831-016-0080-6.

[57] S.C.B. Myneni, S.J. Traina, G. a. Waychunas, T.J. Logan, Vibrational spectroscopy of functional group chemistry and arsenate coordination in ettringite, Geochim. Cosmochim. Acta. 62 (1998) 3499–3514. doi:10.1016/S0016-7037(98)00221-X.

[58] K. Nakamoto, Infrared and raman spectra of inorganic and coordination compounds: Applications in coordination, organometallic, and bioinorganic chemistry, 6th ed., John Wiley & Sons, Hoboken, New Jersey, 2009.

[59] D. Gastaldi, G. Paul, L. Marchese, S. Irico, E. Boccaleri, S. Mutke, L. Buzzi, F. Canonico, Hydration products in sulfoaluminate cements: Evaluation of amorphous phases by XRD/solid-state NMR, Cem. Concr. Res. 90 (2016) 162–173. doi:10.1016/j.cemconres.2016.05.014.

[60] G. Le Saout, E. Lécolier, A. Rivereau, H. Zanni, Chemical structure of cement aged at normal and elevated temperatures and pressures, Cem. Concr. Res. 36 (2004) 71–78. doi:10.1016/j.cemconres.2004.09.018.

[61] T. Matschei, B. Lothenbach, F.P. Glasser, The AFm phase in Portland cement, Cem. Concr. Res. 37 (2007) 118–130. doi:10.1016/j.cemconres.2006.10.010.